

## Effect of sealing treatment on the corrosion behavior of anodized AA2099 aluminum-lithium alloy

Pedro Samaniego-Gómez<sup>a</sup>, Facundo Almeraya-Calderón<sup>a</sup>, Ulises Martín<sup>b</sup>, Jacob Röss<sup>b</sup>, Citlalli Gaona-Tiburcio<sup>a</sup>, Luis Silva-Vidaurre<sup>c</sup>, José Cabral-Miramontes<sup>a</sup>, José M. Bastidas<sup>d</sup>, José G. Chacón-Nava<sup>c</sup>, David M. Bastidas<sup>b,✉</sup>

<sup>a</sup>Universidad Autónoma de Nuevo León. FIME–CIHA, Ave. Universidad s/n, Ciudad Universitaria, 66455 San Nicolás de los Garza, Nuevo León, México

<sup>b</sup>National Center for Education and Research on Corrosion and Materials Performance, NCERCAMP-UA, Dept. Chemical, Biomolecular, and Corrosion Engineering, The University of Akron, 302 E Buchtel Ave, Akron, OH 44325-3906, United States

<sup>c</sup>Centro de Investigación en Materiales Avanzados (CIMAV), Miguel de Cervantes 120, Complejo Industrial Chihuahua, Chihuahua 31136, México

<sup>d</sup>National Center for Metallurgical Research (CENIM, CSIC), Ave. Gregorio del Amo 8, 28040 Madrid, Spain

✉Corresponding author: dbastidas@uakron.edu

Submitted: 18 July 2020; Accepted: 8 October 2020; Available On-line: 14 December 2020

**ABSTRACT:** The corrosion behavior of the sulphuric-anodized AA2099 using two different current densities, 0.19 or 1.0 A·cm<sup>-2</sup>, with two different sealing treatments in H<sub>2</sub>O and 6 wt.% Na<sub>2</sub>Cr<sub>2</sub>O<sub>7</sub> at 95 °C was studied in 3.5 wt.% NaCl and 10 vol.% H<sub>2</sub>SO<sub>4</sub> solutions. The AA2099 is widely used in aeronautical applications, thus it is essential to present good corrosion performance in chloride and acid rain environments. The surface morphology of the anodized film was characterized by scanning electron microscopy (SEM), the electrochemical corrosion behavior was studied using electrochemical impedance (EIS), and finally characterization of the surface chemical composition was revealed by X-ray photoelectron spectroscopy (XPS). It was found the 6 wt.% Na<sub>2</sub>Cr<sub>2</sub>O<sub>7</sub> sealing treatment imparts a more homogeneous and compact passive layer, and tends to increase the charge transfer resistance, thus improving the corrosion behavior of the anodized AA2099.

**KEYWORDS:** Aluminum-lithium AA2099 alloy; Anodizing; Corrosion; Electrochemical impedance; SEM; XPS

**Citation/Citar como:** Samaniego-Gómez, P.; Almeraya-Calderón, F.; Martín, U.; Röss, J.; Gaona-Tiburcio, C.; Silva-Vidaurre, L.; Cabral-Miramontes, J.; Bastidas, J.M.; Chacón-Nava, J.G.; Bastidas, D.M. (2020). "Effect of sealing treatment on the corrosion behavior of anodized AA2099 aluminum-lithium alloy". *Rev. Metal.* 56(4): e180. <https://doi.org/10.3989/revmetalm.180>

**RESUMEN:** Efecto del tratamiento de sellado en el comportamiento frente a corrosión de la aleación anodizada de aluminio-litio AA2099. El comportamiento frente a corrosión de la aleación de aluminio AA2099 anodizado en solución de H<sub>2</sub>SO<sub>4</sub>, aplicando dos densidades de corriente diferentes, 0,19 o 1,0 A·cm<sup>-2</sup>, con dos tratamientos de sellado diferentes en H<sub>2</sub>O y en Na<sub>2</sub>Cr<sub>2</sub>O<sub>7</sub> (6% peso) a 95 °C, se ha estudiado en disoluciones de NaCl (3,5% peso) y de H<sub>2</sub>SO<sub>4</sub> (10% vol). La aleación AA2099 se usa ampliamente en aplicaciones aeronáuticas, por tanto, se requiere que presente un buen comportamiento frente a la corrosión en ambientes de cloruro y lluvia ácida. La morfología de la superficie de la película anodizada se caracterizó por microscopía electrónica de barrido (MEB), se estudió el comportamiento frente a corrosión electroquímica empleando la impedancia electroquímica (EIS), y finalmente la caracterización de la composición química de la superficie se reveló por espectroscopía de fotoelectrones de rayos X (XPS). Se encontró que el tratamiento de sellado con Na<sub>2</sub>Cr<sub>2</sub>O<sub>7</sub> (6% peso), genera una capa pasiva más homogénea y compacta, y tiende a aumentar la resistencia a la transferencia de carga, mejorando así el comportamiento frente a corrosión del AA2099 anodizado.

**PALABRAS CLAVE:** Aleación aluminio-litio AA2099; Anodizado; Corrosión; Impedancia electroquímica; MEB; XPS

**ORCID ID:** Pedro Samaniego-Gómez (<https://orcid.org/0000-0002-6660-4785>); Facundo Almeraya-Calderón (<https://orcid.org/0000-0002-3014-2814>); Ulises Martín (<https://orcid.org/0000-0002-0657-5484>); Jacob Röss (<https://orcid.org/0000-0002-5702-931X>); Citlalli Gaona-Tiburcio (<https://orcid.org/0000-0001-9072-3090>); Luis Silva-Vidaurre (<https://orcid.org/0000-0002-0210-4423>); José Cabral-Miramontes (<https://orcid.org/0000-0003-1483-3081>); José M. Bastidas (<https://orcid.org/0000-0001-9616-0778>); José G. Chacón-Nava (<https://orcid.org/0000-0002-5131-0936>); David M. Bastidas (<https://orcid.org/0000-0002-8720-7500>)

**Copyright:** © 2020 CSIC. This is an open-access article distributed under the terms of the Creative Commons Attribution 4.0 International (CC BY 4.0) License.

## 1. INTRODUCTION

The anodizing process improves the resistance to corrosion and abrasion of Al alloys (AA) by increasing the thickness of the alumina layer ( $\text{Al}_2\text{O}_3$ ) formed. This process involves an electrochemical reaction in acidic electrolytes increasing the thickness of the Al oxide layer. The anodizing process is used mainly for the treatment of Al alloy surfaces for industrial applications. However, in the aeronautic industry, such electrochemical processes are implemented because Al alloys such as 2xxx and 7xxx have a wide range in aerospace applications due to high strength and low density, allowing for an increase in payload and fuel efficiency (Keller *et al.*, 1953; Etienne *et al.*, 2016; Ma *et al.*, 2016; Jaimes-Ramírez *et al.*, 2018; Zhang *et al.*, 2020).

Al-Li AA2099 alloy has been used in the aeronautic industry in recent years due to its low density and high mechanical strength, replacing the conventional 2xxx and 7xxx alloys (Mouritz, 2012; Ma *et al.*, 2016). The chief characteristic of Al-Li alloy is that, by adding 1 wt.% Li, it is possible to decrease the weight by 3% compared to pure Al and the stiffness is increased by 5–6%. Additional advantages of AA2099 include lower in-plane anisotropy of the mechanical properties, greater transverse ductility, excellent resistance to stress corrosion cracking and excellent toughness (Romios *et al.*, 2005; Mouritz, 2012; Deschamps *et al.*, 2013; Ma *et al.*, 2016; Gumbmann *et al.*, 2016a; Gumbmann *et al.*, 2016b; Deng *et al.*, 2017; Deschamps *et al.*, 2017). Due to its low density and high stiffness, Al-Li AA2099 alloy is one of the core materials in aircraft manufacturing applications, for example, in the reinforcement of T-shaped joints for the fuselage panels (Tian *et al.*, 2016). Due to the interaction of Al in contact with the environment, Al alloys form a spontaneous oxide layer on the surface. Such a natural oxide layer does not provide adequate protection in aggressive environments, and Al alloys are susceptible to localized corrosion through microgalvanic coupling between different phases. The high-copper-containing constituent Al-Fe-Mn-Cu particles are responsible for the initiation of localized corrosion in the anodized AA2099 (Ma *et al.*, 2015a). Grains of high stored energy could also contain increased volume fraction of  $\text{Al}_2\text{CuLi}$  intermetallic phase after aging, which might increase corrosion susceptibility (Ma *et al.*, 2015b).

Due to the different conditions that aircraft experience in service, the Al alloys used in the aeronautic industry are anodized before applying primers and topcoats (Ma *et al.*, 2011; Yu *et al.*, 2020; Zhang *et al.*, 2020). By carrying out an anodizing process, it is possible to generate a thicker artificial oxide layer, improving the corrosion resistance, wear resistance and mechanical properties (Runge, 2018). Conversion coatings have proved to impart passivation, such the traditionally applied anodizing

electrolyte containing sulfuric acid, glycerol, lactic acid and titanium dilactate ammonium salt (Dale, 1970). The  $\text{Al}_2\text{O}_3$  layer is characterized by being a compact, fine, porous, and external barrier. The pores act as migration pathways for corrosive agents, therefore a sealing treatment is necessary to stabilize the  $\text{Al}_2\text{O}_3$  layer, thus reducing the diameter of the pores and increasing the corrosion resistance. The sealing treatment can be carried out through different solutions such as water, sodium dichromate ( $\text{Na}_2\text{Cr}_2\text{O}_7$ ), nickel acetate, and nickel fluoride. The efficiency of a sealing process depends on the surface reactivity of the porous oxide structure in the different anodized Al alloys (Etienne *et al.*, 2016; Runge, 2018). Sodium dichromate is considered to be one of the most effective sealing methods for corrosion prevention because it not only blocks pores, it also acts as a corrosion inhibitor, a specific property of self-healing corrosion (Zuo *et al.*, 2003; Etienne *et al.*, 2016; Yu *et al.*, 2020).

The aim of this work is to study the corrosion properties of the Al-Li AA2099 alloy in 3.5 wt.% NaCl and 10 vol.%  $\text{H}_2\text{SO}_4$  solutions. The AA2099 alloy was anodized using a sulfuric acid bath and two current densities, 0.19 and 1.0  $\text{A}\cdot\text{cm}^{-2}$ . A posterior sealing process in  $\text{H}_2\text{O}$  or in  $\text{Na}_2\text{Cr}_2\text{O}_7$  was applied. The resulting specimens were exposed to a 3.5 wt.% NaCl or a 10 vol.%  $\text{H}_2\text{SO}_4$  solution, and their electrochemical corrosion behavior was studied using electrochemical impedance spectroscopy (EIS). Scanning electron microscopy (SEM), and X-ray photoelectron spectroscopy (XPS) analyses were performed to characterize the surface, to determine the morphology, thickness, and chemical composition of the anodized and sealed coatings.

## 2. MATERIALS AND EXPERIMENTAL PROCEDURE

### 2.1. Materials

An Al-Li AA2099 alloy was used as the substrate. The specimens were cut to dimensions of 0.05 m length and 0.005 m in thickness. Specimens were sequentially polished with 400, 600, and 800 SiC grit papers and cleaned with deionized water and acetone.

### 2.2. Anodizing process

Before anodizing, the AA2099 specimens were degreased and etched in a 50% HCl solution for 5 s at 25 °C and rinsed in distilled water (3 times). Anodizing was carried out in a 16 wt.%  $\text{H}_2\text{SO}_4$  solution using two current densities, 0.19 and 1.0  $\text{A}\cdot\text{cm}^{-2}$ , for 45 min at 25 °C. For the sealing process, the anodized specimens were immersed in  $\text{H}_2\text{O}$  at 95 °C temperature for 25 min, or in 6 wt.%  $\text{Na}_2\text{Cr}_2\text{O}_7$  solution at 95 °C temperature for 25 min. Table 1 shows

TABLE 1. Anodizing process parameters and sealing treatments, including nomenclature of the different samples

| Material | Anodizing  |                                     |           | Sealing Treatment                 | Nomenclature |
|----------|--|-------------------------------------|-----------|-----------------------------------|--------------|
|          | Electrolyte  | Current Density, A cm <sup>-2</sup> | Time, min |                                   |              |
| AA2099   | H <sub>2</sub> SO <sub>4</sub>   | 0.19                                | 45        | H <sub>2</sub> O at 95 °C, 25 min | M1           |
|          |  | 1.00                                |           |                                   | M2           |
|          | 6 wt.% Na <sub>2</sub> Cr <sub>2</sub> O <sub>7</sub> at 95 °C, 25 min | 0.19                                | M3        |                                   |              |
|          |  | 1.00                                | M4        |                                   |              |

the nomenclature of the specimens and the variables used in the anodizing and sealing processes.

### 2.3. Electrochemical study

A conventional three-electrode cell configuration was used for the electrochemical study, the anodized AA2099 alloy as working electrode, a saturated calomel electrode (SCE) as reference, and a platinum mesh as counter electrode. Electrochemical measurements were carried out using a Gill-AC potentiostat/galvanostat/ZRA from ACM Instruments (UK). Corrosion experiments were performed by immersion of the anodized and sealed Al-Li AA2099 specimens, with an active surface area of 1.0 cm<sup>2</sup>, in 3.5 wt.% NaCl solution and in 10 vol.% H<sub>2</sub>SO<sub>4</sub> solution, this latter to simulate an acid rain environment, at 25 °C temperature for 3 h. The EIS measurements were recorded at the corrosion potential ( $E_{\text{corr}}$ ) over a frequency range from 100 kHz to 1 mHz, obtaining 10 points per decade, and applying an AC potential signal of 10 mV r.m.s. amplitude according to ASTM G106-89 (2015). The results were analyzed using electrical equivalent circuit (EEC) models and the Zview impedance program. All the EIS tests were performed in triplicate.

### 2.4. Anodized layers characterization

Analysis of in-plane and cross-section surface morphology was done using SEM, in a JEOL JSM 6510LV model operating at an excitation voltage of 20 kV, and a working distance (WD) of 12 mm. Study of the oxide layer thickness of the cross-section was performed at a magnification of 2000X.

X-ray photoelectron spectroscopy (XPS) was used to determine the chemical composition of the Al oxide layer, a Thermo Scientific Escalab 250 Xi equipment was utilized. The pressure in the analysis chamber was maintained below 10<sup>-9</sup> torr. The excitation of the analyzed photoelectrons was carried out with a monochromatic Al K<sub>α</sub> anode X-ray source (1486 eV). The analyzed regions of interest were Al 2p and O 1s. The peaks were fitted using a Gaussian-Lorentzian mixed function, after a Shirley background subtraction (Fajardo *et al.*,

2019). Spectra were obtained at a take-off angle of 45° (Cumpson, 1995).

## 3. RESULTS AND DISCUSSION

### 3.1. SEM, surface and cross-sectional morphologies

The study of the surface and the cross-sectional morphologies of the anodic oxide layer of Al-Li AA2099 alloy is of great importance to understand the corrosion resistance. In Fig. 1, the surface morphology of the anodized AA2099 samples can be observed with varying current density conditions (0.19 and 1.0 A·cm<sup>-2</sup>) and sealing solutions (H<sub>2</sub>O and 6 wt.% Na<sub>2</sub>Cr<sub>2</sub>O<sub>7</sub>) within the anodizing process. Micrographs of the AA2099 show the conventional honeycomb morphology. One of the disadvantages of the Al oxide layer is its porous structure, favoring the accumulation of corrosion products. In order to reduce the Al<sub>2</sub>O<sub>3</sub> layer porosity, two sealing solutions (H<sub>2</sub>O and 6 wt.% Na<sub>2</sub>Cr<sub>2</sub>O<sub>7</sub>) were used to reduce the diameter of the pores. The efficiency of the sealing process depends mainly of the surface reactivity and structure of the passive layer (Etienne *et al.*, 2016; Yang *et al.*, 2019; Yu *et al.*, 2020).

Figure 1(a, c) shows a less homogeneous surface compared to the micrographs of Fig. 1(b, d). This may be due to the amount of current density employed during the anodizing process, resulting in a uniform surface area for the 1.0 A·cm<sup>-2</sup> current density sample. Some imperfections can be observed on the micrographs (see Fig. 1(b, d)). However, the imperfections tend to be in greater abundance on the anodized specimens using current density of 0.19 A·cm<sup>-2</sup> (see Fig. 1(a, c)).

Figure 2 shows the cross-section morphology obtained by SEM of the anodized specimens. For samples anodized using 0.19 A·cm<sup>-2</sup> current density (see Fig. 2(a, c)), a more irregular and cracked oxide layer can be observed, compared to specimens anodized using 1.0 A·cm<sup>-2</sup> current density (see Fig. 2(b, d)) which have a more stable Al<sub>2</sub>O<sub>3</sub> layer. The current density influences the structure of the Al<sub>2</sub>O<sub>3</sub> layer, but not the thickness, as the four specimens have a thickness between 6–9 μm. The specimens anodized using 1.0 A·cm<sup>-2</sup> current density provides greater stability of the Al<sub>2</sub>O<sub>3</sub> layer, as revealed in the micrographs of

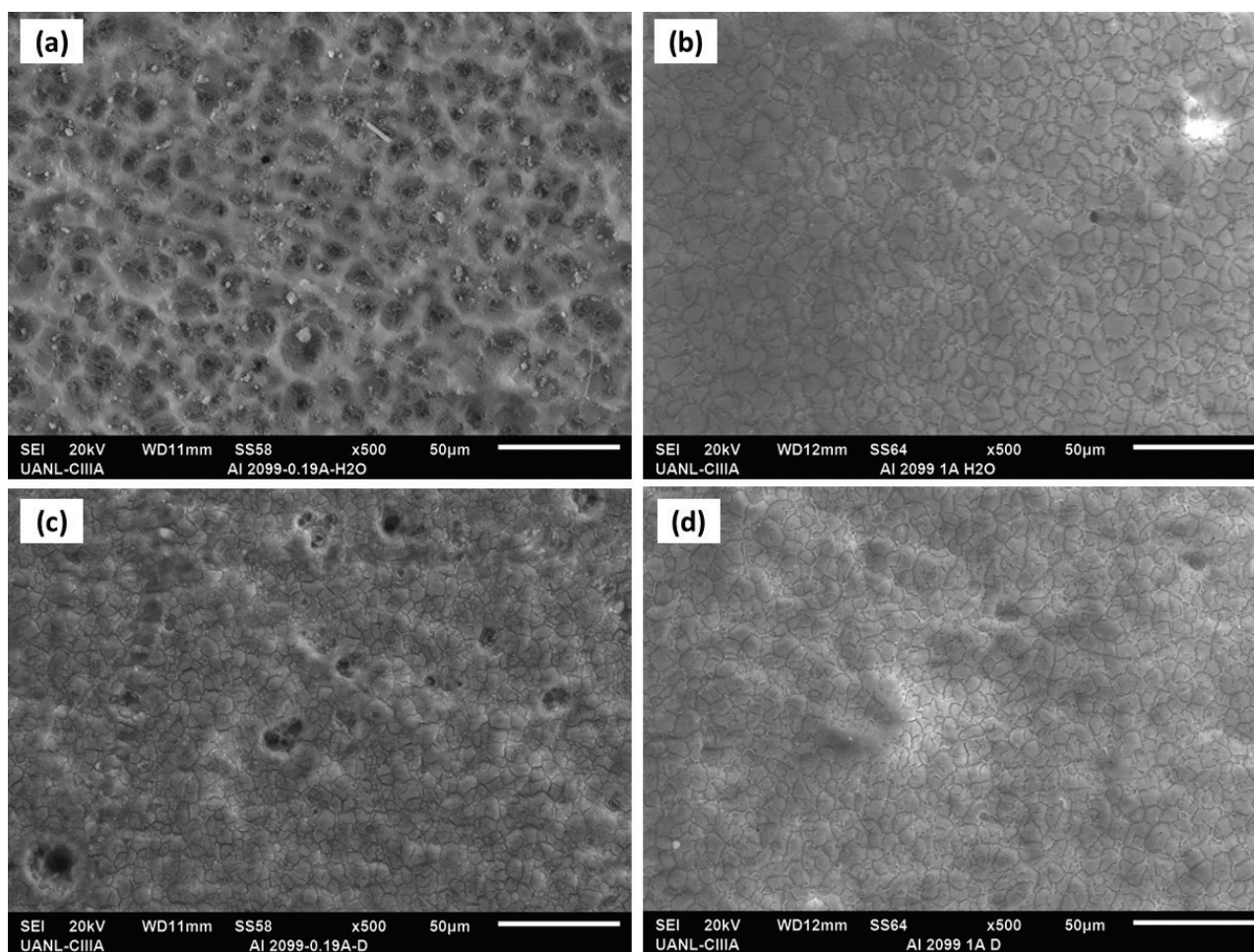


FIGURE 1. SEM micrographs of the in-plane surface morphology of the anodized AA2099 samples with different sealing treatments: (a) M1 ( $\text{H}_2\text{O}$ )/ $0.19 \text{ A}\cdot\text{cm}^{-2}$ , (b) M2 ( $\text{H}_2\text{O}$ )/ $1.0 \text{ A}\cdot\text{cm}^{-2}$ , (c) M3 ( $\text{Na}_2\text{Cr}_2\text{O}_7$ )/ $0.19 \text{ A}\cdot\text{cm}^{-2}$ , and (d) M4 ( $\text{Na}_2\text{Cr}_2\text{O}_7$ )/ $1.0 \text{ A}\cdot\text{cm}^{-2}$ .

Fig. 2(a, c) in which a structure with more imperfections in comparison with the micrographs of Fig. 2(b, d) can be observed. The average thickness obtained in the cross-section of AA2099 specimens sealed in  $\text{H}_2\text{O}$  was  $7.44 \mu\text{m}$ , while for the specimens sealed in 6 wt.%  $\text{Na}_2\text{Cr}_2\text{O}_7$  was  $9.51 \mu\text{m}$ .

### 3.2. EIS data

Figure 3 shows Nyquist plots, along with Bode plots (top-inset) for anodized and sealed AA2099 alloy immersed in 3.5 wt.% NaCl solution for 3 h. For all specimens, a capacitive behavior is observed, as well as a high impedance value ( $>450 \text{ k}\Omega \text{ cm}^2$ ). The best defined semicircle is shown by the M4 specimen ( $1.0 \text{ A}\cdot\text{cm}^{-2}$  current density and 6 wt.%  $\text{Na}_2\text{Cr}_2\text{O}_7$  sealing solution), while the lower impedance was found for the M1 sample, see Fig. 3 bottom inset. The impedance results were fitted using the electrical equivalent circuit (EEC) model in Fig. 4, which includes two-time constants (Yang *et al.*, 2019). The upper inset of Fig. 3 shows the

Bode plots for all impedance data, two peaks can be observed in the phase angle ( $\theta$ ) vs. frequency plot, indicating that AA2099/3.5 wt.% NaCl interface presents two-time constants. This cannot be observed on the Nyquist plots of Fig. 3 because the two-time constants are overlapped. An excellent correlation between the experimental and the fitted data can be observed, see Fig. 3, the fitting procedure matches well with experimental results shown as individual points. Table 2 summarizes the fitting parameters of the EIS data, the  $\chi^2$  values are in the range of  $1.54\text{--}7.92 \times 10^{-3}$ .

The EEC model of Fig. 4 contains the electrolyte resistance ( $R_s$ ), attributed to the ohmic resistance, between the working electrode and the reference electrode.  $R_s$  is in series with a parallel combination ( $R_1//CPE_1$ ) for the high- and intermediate-frequency range response containing the oxide film resistance ( $R_1$ ) and a constant phase element ( $CPE_1$ ), both attributed to the oxide films generated on the AA2099 alloy surface in the anodizing and sealing processes. Additionally,

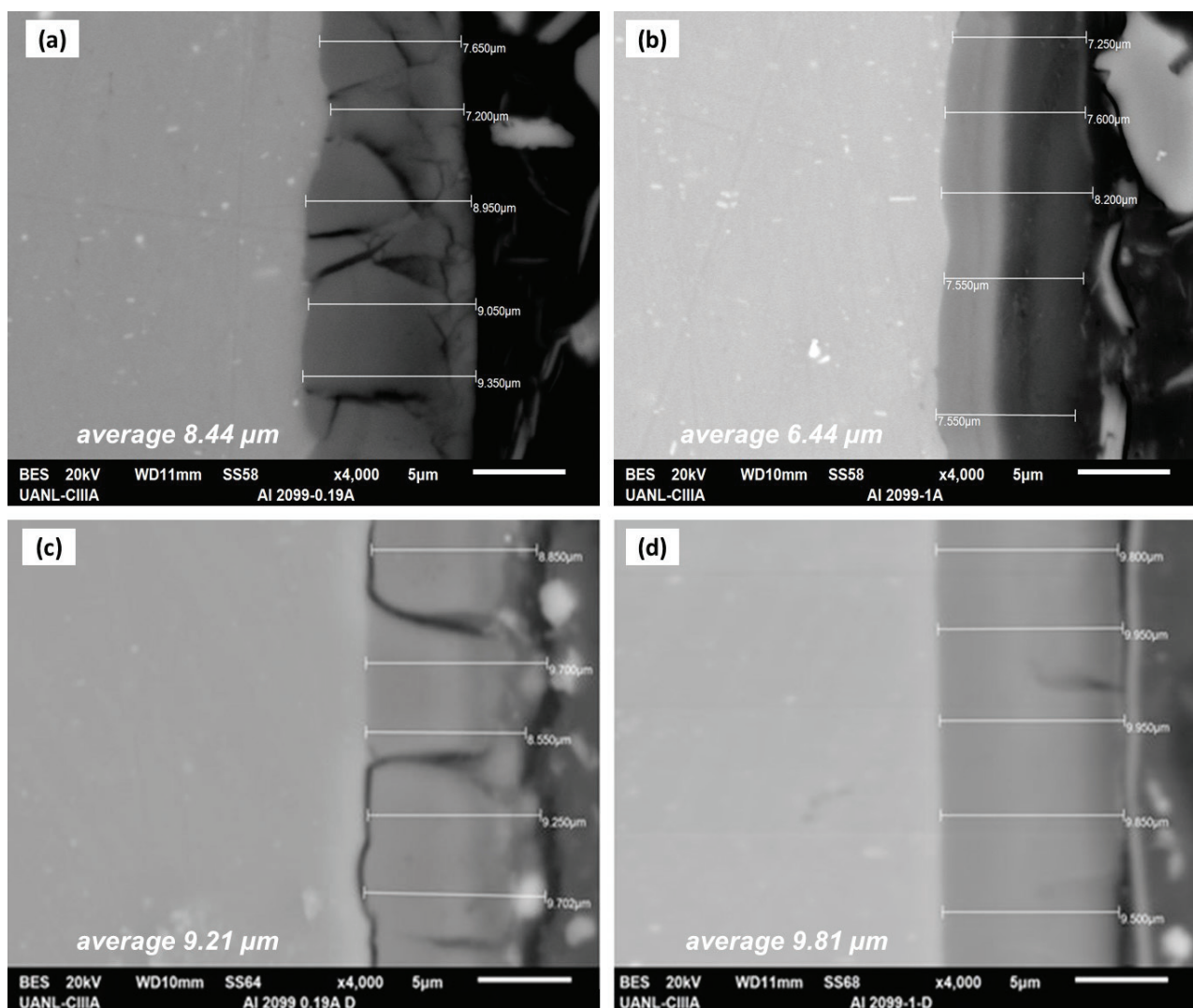


FIGURE 2. SEM micrographs of the cross-section morphology of the anodized AA2099 samples with different sealing treatments: (a) M1 ( $\text{H}_2\text{O}$ )/ $0.19 \text{ A}\cdot\text{cm}^{-2}$ , (b) M2 ( $\text{H}_2\text{O}$ )/ $1.0 \text{ A}\cdot\text{cm}^{-2}$ , (c) M3 ( $\text{Na}_2\text{Cr}_2\text{O}_7$ )/ $0.19 \text{ A}\cdot\text{cm}^{-2}$ , and (d) M4 ( $\text{Na}_2\text{Cr}_2\text{O}_7$ )/ $1.0 \text{ A}\cdot\text{cm}^{-2}$ .

$R_1$  is in series with a second  $R_2//CPE_2$  sub-circuit in parallel, for the low-frequency response measurements, which may be attributed to the corrosion process, where the  $CPE_2$  represents the double-layer capacitance, and the  $R_2$  is the charge transfer resistance, which is inversely proportional to the corrosion rate. A  $CPE$  is defined as an empirical function depending on the frequency and its impedance is defined as:  $Z_{CPE} = (Y)^{-1}(j\omega)^{-n}$ , where  $Y$  is the admittance (a real frequency-independent constant),  $j^2 = (-1)$  is the imaginary number,  $\omega$  is the angular frequency, and  $n$  is a dimensionless fraction exponent ( $-1 < n < +1$ ). When  $n = +1$  the  $CPE$  is an ideal capacitor, and when  $n = -1$  the  $CPE$  is an inductor (Scully *et al.*, 1993; Perez, 2004; Bastidas, 2007; Hirschorn *et al.*, 2010; Jinlong *et al.*, 2016; Evertsson *et al.*, 2017; Ayagou *et al.*, 2018; Halvorsen *et al.*, 2019).

Table 2 shows the four specimens (M1–M4) have a similar  $R_s$  value in the range of  $29.38\text{--}33.65 \Omega \text{ cm}^2$ . The value of the dielectric properties of the oxide films generated on the anodized and sealed AA2099 alloy surface, which correspond to the admittance ( $Y_1$ ) in the  $CPE_1$  (Bastidas, 2007), were found to be of the same order of magnitude for each specimen ( $1.07\text{--}2.06 \mu\text{S}\cdot\text{cm}^{-2} \text{ s}^{n1}$ ), indicating protective properties. The  $R_1$  parameter for each specimen was found to be of the same order of magnitude, except for the specimen M3 ( $0.19 \text{ A}\cdot\text{cm}^{-2}$  current density, and 6 wt.%  $\text{Na}_2\text{Cr}_2\text{O}_7$  sealing solution) having a  $R_1$  value one order of magnitude lower ( $750.5 \Omega \text{ cm}^2$ ). This behavior is observed because the 6 wt.%  $\text{Na}_2\text{Cr}_2\text{O}_7$  solution does not reduce the diameter of the pores, therefore it behaves as a corrosion inhibitor by a precipitation mechanism inside the pores, which hinders the corrosion process and causes cracking,

as was observed in Fig. 2c (Zuo *et al.*, 2003; Yang *et al.*, 2019). The  $n_1$  parameter presents high values inducing non-depressed semicircles, which indicates

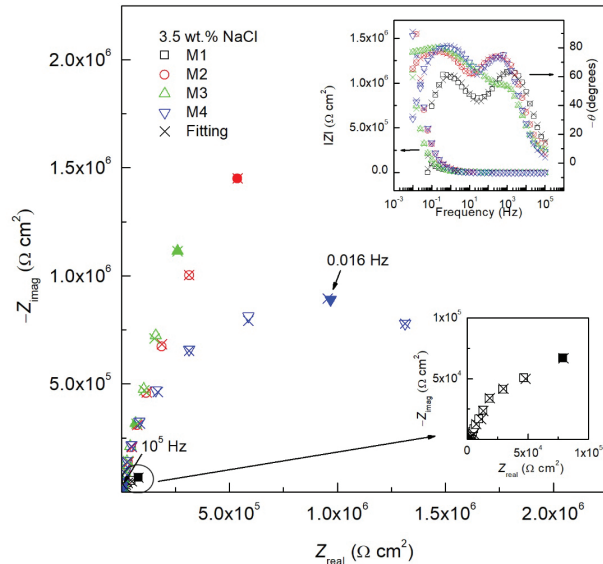


FIGURE 3. Nyquists plots of anodized AA2099 samples with different sealing treatments (M1, M2, M3 and M4) exposed to 3.5 wt.% NaCl, showing top-inset Bode plots, and bottom-inset magnified Nyquist plot of M1 sample.

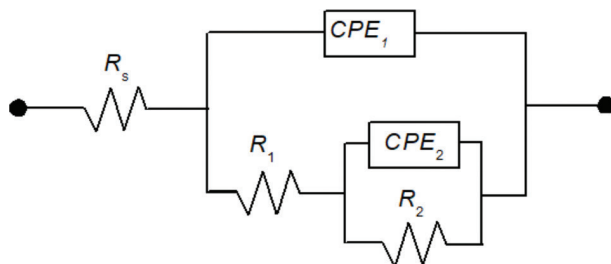


FIGURE 4. Electrical equivalent circuit (EEC) used to fit EIS data, comprising series resistance ( $R_s$ ) and two-time constants  $CPE_1//R_1$  and  $CPE_2//R_2$ .

a homogeneous oxide film surface (Djellab *et al.*, 2019). Figure 3 shows that the smallest defined semi-circle was found for the sample M1 ( $0.19 \text{ A}\cdot\text{cm}^{-2}$  current density, and deionized water sealing solution) having a  $R_2$  value one order of magnitude lower ( $178.32 \text{ } \Omega \text{ cm}^2$ ) than M2, M3 and M4 samples (see Table 2). The effect of water as a sealing solution is to produce a reduction of the porous diameter of the honeycomb structure, probably the  $0.19 \text{ A}\cdot\text{cm}^{-2}$  current density presents some limitations generating a low corrosion resistant oxide film. The capacitance of the electrochemical double-layer ( $Y_2$ ) was in the range of  $1.14\text{--}4.33 \text{ } \mu\text{S}\cdot\text{cm}^{-2} \text{ s}^{n_2}$ , and the  $n_2$  parameter presented high values ( $0.80\text{--}0.97$ ), very close to an ideal-capacitor behavior ( $n=1$ ), see Table 2.

Figure 5 shows Nyquist plots for anodized and sealed AA2099 alloy immersed in 10 vol.%  $\text{H}_2\text{SO}_4$

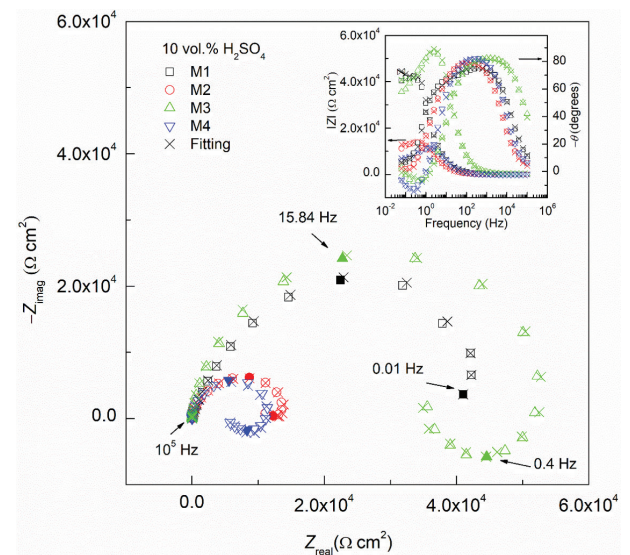


FIGURE 5. Nyquists plots of anodized AA2099 samples with different sealing treatments (M1, M2, M3 and M4) exposed to 10 vol.%  $\text{H}_2\text{SO}_4$ , showing inset Bode plots.

TABLE 2. EIS fitting data for anodized and sealed AA2099 samples exposed to 3.5 wt.% NaCl and 10 vol.%  $\text{H}_2\text{SO}_4$  solutions for 3 h

| Sample   | $R_s \text{ } \Omega \text{ cm}^2$ | $Y_1 \text{ } \mu\text{S cm}^{-2} \text{ s}^{n_1}$ | $n_1$ | $R_1 \text{ } \Omega \text{ cm}^2$ | $Y_2 \text{ } \mu\text{S cm}^{-2} \text{ s}^{n_2}$ | $n_2$ | $R_2 \text{ k}\Omega \text{ cm}^2$ | $\chi^2$              |
|--|------------------------------------|--|-------|------------------------------------|--|-------|------------------------------------|-----------------------|
| <b>3.5 wt.% NaCl</b>                               |                                    |  |       |                                    |  |       |                                    |                       |
| M1   | 29.38                              | 1.25   | 0.80  | 3669                               | 4.33   | 0.80  | 178.32                             | $2.57 \times 10^{-3}$ |
| M2   | 31.02                              | 1.07   | 0.88  | 12039.5                            | 1.28   | 0.88  | 9295.45                            | $3.22 \times 10^{-3}$ |
| M3   | 33.65                              | 2.06   | 0.86  | 750.5                              | 3.09   | 0.87  | 41453.45                           | $7.92 \times 10^{-3}$ |
| M4   | 32.25                              | 1.15   | 0.91  | 5638                               | 1.14   | 0.97  | 1977.16                            | $1.54 \times 10^{-3}$ |
| <b>10 vol.% <math>\text{H}_2\text{SO}_4</math></b> |                                    |  |       |                                    |  |       |                                    |                       |
| M1   | 11.31                              | 1.72   | 0.87  | 11005.5                            | -5.28  | 0.49  | -40.80                             | $1.44 \times 10^{-3}$ |
| M2   | 11.27                              | 2.84   | 0.92  | 3776                               | -36.17   | 0.53  | -20.39                             | $9.94 \times 10^{-3}$ |
| M3   | 11.21                              | 0.15   | 0.93  | 32285.5                            | -18.88   | 0.61  | -12.28                             | $2.17 \times 10^{-3}$ |
| M4   | 11.31                              | 1.31   | 0.95  | 6632.5                             | -91.02   | 0.41  | -4.99                              | $1.73 \times 10^{-3}$ |

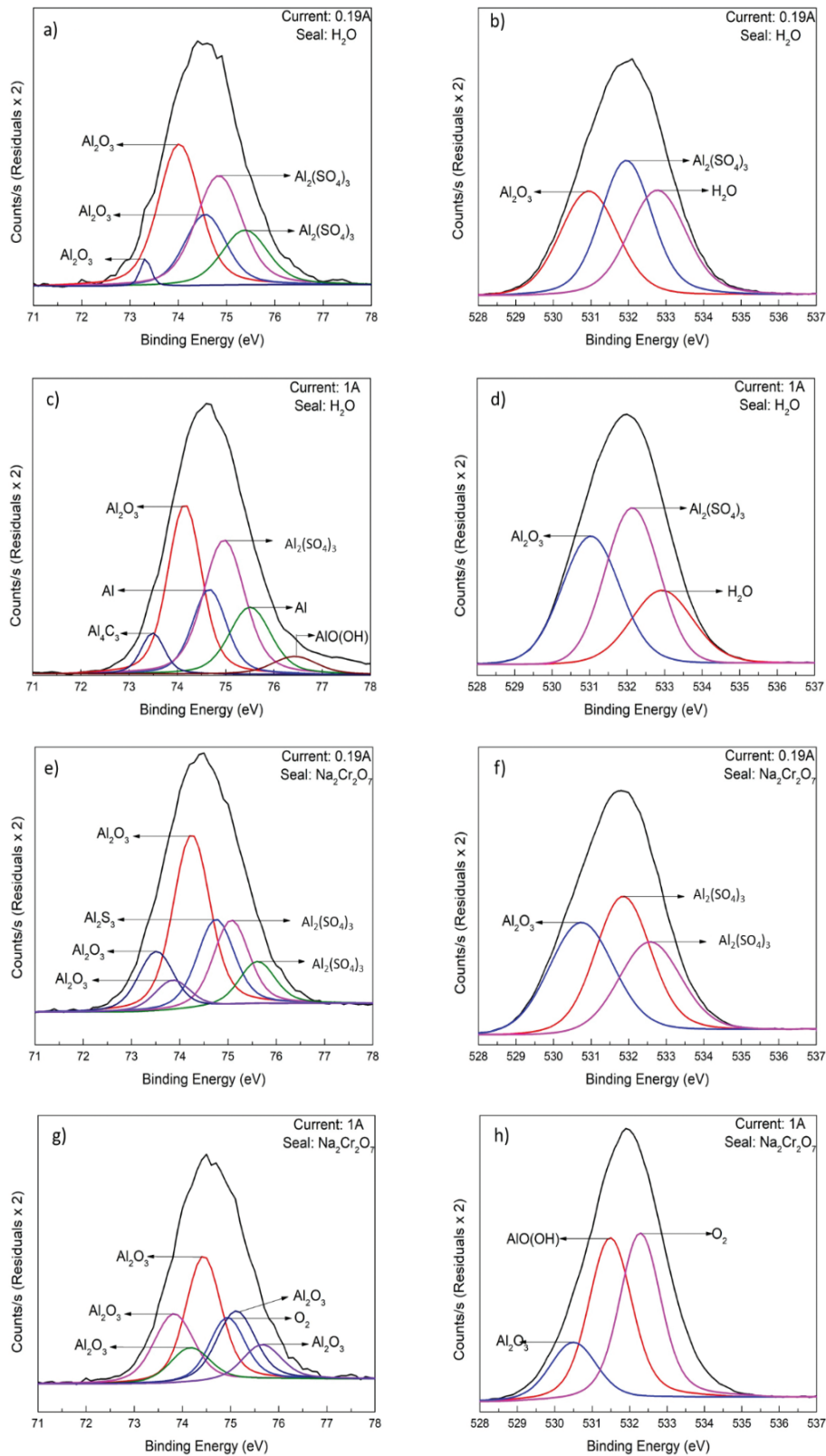


FIGURE 6. High resolution XPS spectra of anodized AA2099 samples with different sealing treatments: (a) element Al 2p for M1, (b) element O 1s for M1, (c) Al 2p for M2, (d) O 1s for M2, (e) Al 2p for M3, (f) O 1s for M3, (g) Al 2p for M4, and (h) O 1s for M4.

solution for 3 h. The four Nyquist plots show the same trend, a depressed capacitive loop behavior from high- to intermediate-frequency, and a depressed inductive loop at low-frequencies in the fourth quadrant. The inset of Fig. 5 shows the Bode plots. The impedance results were fitted using the EEC of Fig. 4, having two-time constants as indicated above, where  $R_s$ ,  $CPE_1$ , and  $R_1$  have the same meaning as Fig. 3, and the  $R_2//CPE_2$  sub-circuit is associated with the inductive loop, which may be explained by the possible adsorption on the AA2099 alloy surface of some species such as  $H^+$  and/or  $SO_4^{2-}$  generated in the aggressive 10 vol.%  $H_2SO_4$  medium (Pivac and Barbir, 2016; Djellab *et al.*, 2019; Klotz, 2019). This process was simulated with  $CPE_2$  and  $R_2$  parameters having negative values. Negative capacitance ( $Y_2$ ) and resistance ( $R_2$ ) arise from surface coverage and adsorption-desorption processes, respectively (Bastidas *et al.*, 2001; Jinlong *et al.*, 2016; Jirón-Lazos *et al.*, 2018). The highest  $R_1$  value was obtained for the specimen M3 ( $32285.5 \Omega \text{ cm}^2$ ) (see Table 2), showing allows the precipitation mechanism of dichromate acting as a corrosion inhibitor on the porous  $Al_2O_3$  layer. The corrosion inhibition observed for treated AA2099 alloys can be primarily attributed to the reduction of the active surface area by the anodized layer (Ardelean *et al.*, 2009). The  $n_1$  parameter value is high (0.87–0.95), meaning a homogeneous surface of the anodic oxide layer. It can be observed on Fig. 5 that  $R_2$  value for M1 and M2 specimens ( $-40.80$  and  $-20.39 \text{ k}\Omega \text{ cm}^2$ ) is the highest, which may be attributed to a reduction in the diameter of the pores of the anodic oxide layer (Zuo *et al.*, 2003; Yang *et al.*, 2019). The  $n_2$  parameter presents low values (see Table 2), producing depressed semi-circles, which may be attributed to the heterogeneity of the surface or to the interfacial phenomena (Djellab *et al.*, 2019).

### 3.3. XPS surface analysis

XPS experiments were performed to determine the chemical composition of the oxide layer generated by anodizing using 0.19 or 1.0  $A \cdot \text{cm}^{-2}$  current density, and sealing using  $H_2O$  or 6 wt.%  $Na_2Cr_2O_7$  solution, on the AA2099 alloy. Figure 6 (a-h) shows high resolution XPS spectra for Al 2p and O 1s. Spectra for Al 2p shows five chemical species assigned to  $Al_2O_3$ ,  $Al_2S_3$ ,  $Al_2(SO_4)_3$ ,  $AlO(OH)$  and  $Al_4C_3$ , (74.5 eV binding energy), and metallic Al, see Fig. 6 (a, c, e, g). The XPS spectra of O 1s reveal the typical binding energies for O 1s, 531.0–532.5 eV (Romios *et al.*, 2005; Pérez *et al.*, 2010; Abrahami *et al.*, 2015), see Fig. 6 (b, d, f, h). In the current study Cr 2p<sub>3/2</sub> signal was not detected, according to Jaimes-Ramirez *et al.* (2018), this may be due to a migration process of the chromate ions into the interior of the

$Al_2O_3$  layer (Jaimes-Ramirez *et al.*, 2018). AA2099 specimens sealed in  $H_2O$  presented a surface film rich in  $Al_2(SO_4)_3$ , this is attributed to the initial  $H_2SO_4$  anodizing process, while for the  $Na_2Cr_2O_7$  sealing the  $AlO(OH)$  was the main oxyhydroxide found on the surface. Among the results, it is possible to observe compounds where the presence of significant amounts of C is found on the surface of the oxide layer, which may be attributed to the accumulation of pollutants during exposure to air (Skeldon *et al.*, 1997; Ryu *et al.*, 1999; Romios *et al.*, 2005; Liou *et al.*, 2013; Abrahami *et al.*, 2015; Khan *et al.*, 2019).

## 4. CONCLUSIONS

- AA2099 samples anodized using a 0.19  $A \cdot \text{cm}^{-2}$  current density presented more irregular and cracked oxide layer than using a 1.0  $A \cdot \text{cm}^{-2}$  current density.
- The EIS results revealed that the  $Na_2Cr_2O_7$  solution has an increased charge transfer resistance in a less homogeneous and less compact  $Al_2O_3$  layer, thus it is possible to filter these imperfections, protecting the substrate (AA2099) by corrosion-inhibitor-like behavior.
- By generating a more homogeneous and compact anodic oxide layer, it benefits the charge transfer resistance by preventing the  $Cl^-$  ingress into the passive  $Al_2O_3$  layer.
- The 10 wt.%  $H_2SO_4$  electrolyte solutions benefit the development of the adsorption-desorption processes on the anodized and sealed alloy surface, resulting in an inductive loop observed for all the samples exposed in  $H_2SO_4$  electrolyte.
- The XPS technique revealed that the surface film consists of a mixture of chemical compounds, mainly formed by  $Al_2O_3$ ,  $AlO(OH)$  and  $Al_2(SO_4)_3$ .

## ACKNOWLEDGEMENTS

The authors would like to thank the Mexican National Council for Science and Technology (CONACYT) for the support provided for the development of the projects CB 253272 and A1-S-8882, the UANL-CA-316 working group and Universidad Autónoma de Nuevo León (UANL) for the facilities given to develop this investigation. U. Martin, J. Ress and D.M. Bastidas acknowledge funding from Firestone Research Grant 639430 and The University of Akron.

## Conflict of Interest

The authors declare that they have no conflict of interest.

## REFERENCES

- Abrahami, S.T., Hauffman, T., de Kok, J.M.M., Mol, J.M.C., Terryn, H. (2015). XPS Analysis of the surface chemistry and interfacial bonding of barrier-type Cr(VI)-free anodic oxides. *J. Phys. Chem. C* 119 (34), 19967–19975. <https://doi.org/10.1021/acs.jpcc.5b05958>.
- Ardelean, H., Frateur, I., Zanna, S., Atrens, A., Marcus, P. (2009). Corrosion protection of AZ91 magnesium alloy by anodizing in niobium and zirconium-containing electrolytes. *Corros. Sci.* 51 (12), 3030–3038. <https://doi.org/10.1016/j.corsci.2009.08.030>.
- ASTM G106-89 (2015). Standard practice for verification of algorithm and equipment for electrochemical impedance measurements. ASTM International, West Conshohocken, PA USA.
- Ayagou, M.D.D., Tran, T.T.M., Tribollet, B., Kittel, J., Sutter, E., Ferrando, N., Mendibide, C., Duret-Thual, C. (2018). Electrochemical impedance spectroscopy of iron corrosion in H<sub>2</sub>S solutions. *Electrochim. Acta* 282, 775–783. <https://doi.org/10.1016/j.electacta.2018.06.052>.
- Bastidas, D.M. (2007). Interpretation of impedance data for porous electrodes and diffusion processes. *Corrosion* 63 (6), 515–521. <https://doi.org/10.5006/1.3278402>.
- Bastidas, J.M., Polo, J.L., Torres, C.L., Cano, E. (2001). A study on the stability of AISI 316L stainless steel pitting corrosion through its transfer function. *Corros. Sci.* 43 (2), 269–281. [https://doi.org/10.1016/S0010-938X\(00\)00082-2](https://doi.org/10.1016/S0010-938X(00)00082-2).
- Cumpson, P.J. (1995). Angle-resolved XPS and AES: Depth-resolution limits and a general comparison of properties of depth-profile reconstruction methods. *J. Electron Spectrosc. Relat. Phenom.* 73 (1), 25–52. [https://doi.org/10.1016/0368-2048\(94\)02270-4](https://doi.org/10.1016/0368-2048(94)02270-4).
- Dale, K.H. (1970). Anodizing aluminum. Patent US3524799A.
- Deng, Y., Bai, J., Wu, X., Huang, G., Cao, L., Huang, L. (2017). Investigation on formation mechanism of Ti precipitate in an Al-Cu-Li alloy. *J. Alloys Compd.* 723, 661–666. <https://doi.org/10.1016/j.jallcom.2017.06.198>.
- Deschamps, A., Decreus, B., De Geuser, F., Dorin, T., Weyland, M. (2013). The influence of precipitation on plastic deformation of Al-Cu-Li alloys. *Acta Mater.* 61 (11), 4010–4021. <https://doi.org/10.1016/j.actamat.2013.03.015>.
- Deschamps, A., Garcia, M., Chevy, J., Davo, B., De Geuser, F. (2017). Influence of Mg and Li content on the microstructure evolution of Al-Cu-Li alloys during long-term ageing. *Acta Mater.* 122, 32–46. <https://doi.org/10.1016/j.actamat.2016.09.036>.
- Djellab, M., Bentrach, H., Chala, A., Taoui, H. (2019). Synergistic effect of halide ions and gum arabic for the corrosion inhibition of API5L X70 pipeline steel in H<sub>2</sub>SO<sub>4</sub>. *Mater. Corros.* 70 (1), 149–160. <https://doi.org/10.1002/maco.201810203>.
- Etienne, M., Rocca, E., Chahboun, N., Veys-Renaux, D. (2016). Local evolution of pH with time determined by shear force-based scanning electrochemical microscopy: Surface reactivity of anodized aluminium. *Electroanalysis* 28 (10), 2466–2471. <https://doi.org/10.1002/elan.201600294>.
- Evertsson, J., Bertram, F., Rullik, L., Harlow, G., Lundgren, E. (2017). Anodization of Al(100), Al(111) and Al Alloy 6063 studied in situ with X-ray reflectivity and electrochemical impedance spectroscopy. *J. Electroanal. Chem.* 799, 556–562. <https://doi.org/10.1016/j.jelechem.2017.07.010>.
- Fajardo, S., Llorente, I., Jiménez, J.A., Bastidas, J.M., Bastidas, D.M. (2019). Effect of Mn additions on the corrosion behaviour of TWIP Fe-Mn-Al-Si austenitic steel in chloride solution. *Corros. Sci.* 154, 246–253. <https://doi.org/10.1016/j.corsci.2019.04.026>.
- Gumbmann, E., De Geuser, F., Deschamps, A., Lefebvre, W., Robaut, F., Sigli, C. (2016a). A combinatorial approach for studying the effect of Mg concentration on precipitation in an Al-Cu-Li alloy. *Scripta Mater.* 110, 44–47. <https://doi.org/10.1016/j.scriptamat.2015.07.042>.
- Gumbmann, E., Lefebvre, W., De Geuser, F., Sigli, C., Deschamps, A. (2016b). The effect of minor solute additions on the precipitation path of an Al-Cu-Li alloy. *Acta Mater.* 115, 104–114. <https://doi.org/10.1016/j.actamat.2016.05.050>.
- Halvorsen, I.J., Pivac, I., Bezmalinović, D., Barbir, F., Zenith, F. (2019). Electrochemical low-frequency impedance spectroscopy algorithm for diagnostics of PEM fuel cell degradation. *Int. J. Hydrog. Energy* 45 (2), 1325–1334. <https://doi.org/10.1016/j.ijhydene.2019.04.004>.
- Hirschorn, B., Orazem, M.E., Tribollet, B., Vivier, V., Frateur, I., Musiani, M. (2010). Determination of effective capacitance and film thickness from constant-phase-element parameters. *Electrochim. Acta* 55 (21), 6218–6227. <https://doi.org/10.1016/j.electacta.2009.10.065>.
- Jaimes-Ramírez, R., Covelo, A., Rodil, S.E., Corona-Lira, P., Ramírez-Reivich, A.C., Hernández, M. (2018). Development and characterization of hydrophobic anodized aluminum layer to act as a long-lasting protective film in corrosion. *Surf. Interface Anal.* 50 (11), 1030–1035. <https://doi.org/10.1002/sia.6437>.
- Jinlong, L., Tongxiang, L., Chen, W., Ting, G. (2016). The passive film characteristics of several plastic deformation 2099 Al-Li alloy. *J. Alloys Compd.* 662, 143–149. <https://doi.org/10.1016/j.jallcom.2015.12.051>.
- Jirón-Lazos, U., Corvo, F., De la Rosa, S.C., García-Ochoa, E.M., Bastidas, D.M., Bastidas, J.M. (2018). Localized corrosion of aluminum alloy 6061 in the presence of *Aspergillus niger*. *Int. Biodeter. Biodegr.* 133, 17–25. <https://doi.org/10.1016/j.ibiod.2018.05.007>.
- Keller, F., Hunter, M.S., Robinson, D.L. (1953). Structural features of oxide coatings on aluminum. *J. Electrochem. Soc.* 100, 411–419. <https://doi.org/10.1149/1.2781142>.
- Khan, M.F., Kumar, A.M., Ul-Hamid, A., Al-Hems, L.M. (2019). Achieving non-adsorptive anodized film on Al-2024 alloy: Surface and electrochemical corrosion investigation. *Surf. Interfaces* 15, 78–88. <https://doi.org/10.1016/j.surfint.2019.02.005>.
- Klotz, D. (2019). Negative capacitance or inductive loop? – A general assessment of a common low frequency impedance feature. *Electrochem. Commun.* 98, 58–62. <https://doi.org/10.1016/j.elecom.2018.11.017>.
- Liou, Y.-J., Chen, Y.J., Chen, B.-R., Lee, L.-M., Huang, C.-H. (2013). XPS study of aluminum coating on TiO<sub>2</sub> anode of dye-sensitized solar cells. *Surf. Coat. Tech.* 231, 535–538. <https://doi.org/10.1016/j.surfcoat.2012.02.008>.
- Ma, Y., Zhou, X., Thompson, G.E., Curioni, M., Zhong, X., Koroleva, E., Skeldon, P., Thomson, P., Fowles, M. (2011). Discontinuities in the porous anodic film formed on AA2099-T8 aluminium alloy. *Corros. Sci.* 53 (12), 4141–4151. <https://doi.org/10.1016/j.corsci.2011.08.023>.
- Ma, Y., Chen, X., Zhou, X., Yi, Y., Liao, Y., Huang, W. (2015a). Microstructural origin of localized corrosion in anodized AA2099-T8 aluminium-lithium alloy. *Surf. Interface Anal.* 48 (8), 739–744. <https://doi.org/10.1002/sia.5856>.
- Ma, Y., Zhou, X., Huang, W., Liao, Y., Chen, X., Zhang, X., Thompson, G.E. (2015b). Crystallographic defects induced localised corrosion in AA2099-T8 aluminium alloy. *Corros. Eng. Sci. Technol.* 50 (6), 420–424. <https://doi.org/10.1179/1743278214Y.00000000237>.
- Ma, Y.-L., Zhou, X.-R., Meng, X.-M., Huang, W.-J., Liao, Y., Chen, X.-L., Yi, Y.-N., Zhang, X.-X., Thompson, G.E. (2016). Influence of thermomechanical treatments on localized corrosion susceptibility and propagation mechanism of AA2099 Al-Li alloy. *T. Nonferr. Metal. Soc. China* 26 (6), 1472–1481. [https://doi.org/10.1016/S1003-6326\(16\)64252-8](https://doi.org/10.1016/S1003-6326(16)64252-8).
- Mouritz, A.P. (2012). *Introduction to Aerospace Materials*. Woodhead Publishing, PA, USA.
- Pérez, N. (2004). *Electrochemistry and Corrosion Science*. Springer, NY, USA.
- Pérez, O.E.L., Sánchez, M.D., Teijelo, M.L. (2010). Characterization of growth of anodic antimony oxide films by ellipsometry and XPS. *J. Electroanal. Chem.* 645 (2), 143–148. <https://doi.org/10.1016/j.jelechem.2010.04.023>.
- Pivac, I., Barbir, F. (2016). Inductive phenomena at low frequencies in impedance spectra of proton exchange membrane fuel cells – A review. *J. Power Sources* 326, 112–119. <https://doi.org/10.1016/j.jpowsour.2016.06.119>.

- Romios, M., Tiraschi, R., Ogren, J.R., Es-Said, O.S., Parrish, C., Babel, H.W. (2005). Design of multistep aging treatments of 2099 (C458) Al-Li alloy. *J. Mater. Eng. Perform.* 14, 641–646. <https://doi.org/10.1361/105994905X64594>.
- Runge, J.M. (2018). *The Metallurgy of Anodizing Aluminum*. Springer, Chicago, USA.
- Ryu, S.-K., Park, B.-J., Park, S.-J. (1999). XPS Analysis of Carbon Fiber Surfaces—Anodized and Interfacial Effects in Fiber-Epoxy Composites. *J. Colloid Interface Sci.* 215 (1), 167–169. <https://doi.org/10.1006/jcis.1999.6240>.
- Scully, J.R., Silverman, D.C., Kendig, M.W. (1993). *Electrochemical impedance: Analysis and interpretation*. STP 1188. ASTM International, USA. <https://doi.org/10.1520/STP1188-EB>.
- Skeldon, P., Wang, H.W., Thompson G.E. (1997). Formation and characterization of self-lubricating MoS<sub>2</sub> precursor films on anodized aluminium. *Wear* 206 (1–2), 187–196. [https://doi.org/10.1016/S0043-1648\(96\)07350-4](https://doi.org/10.1016/S0043-1648(96)07350-4).
- Tian, Y., Robson, J.D., Riekehr, S., Kashaev, N., Wang, L., Lowe, T., Karanika, A. (2016). Process optimization of dual-laser beam welding of advanced Al-Li alloys through hot cracking susceptibility modeling. *Metall. Mater. Trans. A* 47, 3533–3544. <https://doi.org/10.1007/s11661-016-3509-4>.
- Yang, Y., Cheng, J., Liu, S., Wang, H., Dong, P. (2019). Effect of NaAlO<sub>2</sub> sealing on corrosion resistance of 2024 aluminum alloy anodized film. *Mater. Corros.* 70 (1), 120–127. <https://doi.org/10.1002/maco.201810327>.
- Yu, S., Wang, L., Wu, C., Feng, T., Cheng, Y., Bu, Z., Zhu, S. (2020). Studies on the corrosion performance of an effective and novel sealing anodic oxide coating. *J. Alloys Compd.* 817, 153257. <https://doi.org/10.1016/j.jallcom.2019.153257>.
- Zhang, F., Örnek, C., Nilsson, J.O., Pan, J. (2020). Anodisation of aluminium alloy AA7075—Influence of intermetallic particles on anodic oxide growth. *Corros. Sci.* 164, 108319. <https://doi.org/10.1016/j.corsci.2019.108319>.
- Zuo, Y., Zhao, P.H., Zhao, J.M. (2003). The influences of sealing methods on corrosion behavior of anodized aluminum alloys in NaCl solutions. *Surf. Coat. Technol.* 166, 237–242. [https://doi.org/10.1016/S0257-8972\(02\)00779-X](https://doi.org/10.1016/S0257-8972(02)00779-X).